

Quantum Simulation of Bound and Resonant Doubly-Bottom Tetraquark

Ayanendu Dutta^{1, 2, *}

¹*Department of Physics, Jadavpur University, Kolkata-700032, India*

²*Department of Physics, Presidency University, Kolkata-700073, India*

We present the first quantum-simulation study of bound and resonant doubly-bottom tetraquark states within a QCD-inspired chiral quark model. An effective four-quark Hamiltonian is mapped onto a 16-qubit register, encoding color, spin, and spatial degrees of freedom, and incorporating both meson-meson and diquark-antidiquark configurations with complete color bases. Using a variational quantum eigensolver, we identify bound and resonance states in the low-lying S -wave sector. Deeply bound states are found exclusively in the isoscalar $I(J^P) = 0(1^+)$ channel, dominated by color-singlet meson-meson components with non-negligible hidden-color contributions. The resulting masses and binding energies are consistent with classical chiral quark model predictions, establishing quantum simulation as a viable framework for studying exotic multiquark states beyond the reach of conventional methods.

I. INTRODUCTION

Over roughly the last two decades, a large number of unconventional charmonium-like and bottomonium-like states, collectively referred to as the XYZ mesons, have been reported in a variety of experimental settings. These states have been observed at B-factories such as BABAR, Belle, and CLEO; at τ -charm experiments including CLEO-c and BESIII; as well as at proton and proton-antiproton collider experiments, notably CDF, D0, LHCb, ATLAS, and CMS. Representative discoveries include the $Y(4260)$ reported by the BABAR Collaboration in 2005 [1], the charged state $Z^+(4430)$ observed by Belle in 2007 [2], the $Y(4140)$ identified by CDF in 2009 [3], and the $Z_c^+(3900)$ discovered by BESIII in 2013 [4], among many others.

These observations have triggered intense theoretical interest in exotic hadrons that extend beyond the conventional quark-antiquark and three-quark picture. In the fully heavy sector, a possible $bbbb$ tetraquark signal was suggested by the CMS Collaboration through $\Upsilon(1S)$ pair production in pp collisions at the LHC [5], with a mass around 18.4 GeV, and a peak near 18.2 GeV was reported in Cu+Au collisions at RHIC [6], while no supporting evidence was found by LHCb in searches of the $\Upsilon(1S)\mu^+\mu^-$ invariant mass spectrum [7]. Theoretically, fully heavy tetraquark systems $QQ\bar{Q}\bar{Q}$ ($Q = c, b$) have been studied using phenomenological models, QCD sum rules, Bethe-Salpeter equations, diffusion Monte Carlo methods, and lattice QCD. While several approaches predict bound or narrow $bbbb$ and $cccc$ states [8–18], other studies find no evidence for such bound states [19–25], leaving the existence of fully heavy tetraquarks an open and actively debated issue, with mixed-flavor systems such as $bb\bar{b}\bar{c}$ and $b\bar{c}\bar{b}\bar{c}$ remaining viable candidates [19, 20].

Theoretical studies of doubly-heavy tetraquark systems exhibit a higher degree of consistency. In the heavy-quark limit, the existence of a stable and extremely nar-

row $bb\bar{u}\bar{d}$ tetraquark with $J^P = 1^+$ is expected [26]. A mass of 10389 ± 12 MeV for the same spin-parity configuration was predicted in Ref. [27], while its mass spectrum, lifetime, and decay properties were analyzed in Ref. [28]. Evidence for a compact doubly-bottom tetraquark with $IJ^P = 01^+$ has also been discussed in the context of heavy-ion collisions at the LHC [29]. Notably, the $T(b\bar{b}\bar{u}\bar{d})$ dimeson was already proposed several decades ago [30]. In addition, a narrow diquark-antidiquark configuration $(bb)(\bar{u}\bar{d})$ with $IJ^P = 01^+$ has been predicted [31]. Lattice QCD calculations further support a deeply bound $\bar{b}b\bar{u}\bar{d}$ state with identical quantum numbers, stable against strong and electromagnetic decays, with a mass of $10476 \pm 24 \pm 10$ MeV [32], consistent with earlier studies using similar frameworks [33, 34].

In this work, we investigate the existence of bound and resonant tetraquark states in the doubly-bottom sector within the complex-scaling framework of the chiral quark model. States with quantum numbers $J^P = 0^+$ and 1^+ are examined in both isospin $I = 0$ and $I = 1$ channels. Two possible internal configurations are considered: meson-meson and diquark-antidiquark structures. For the meson-meson picture, both color-singlet and hidden-color channels are included, while the diquark-antidiquark configuration incorporates color triplet-antitriplet and sextet-antisextet channels, together with their mutual couplings. Previous calculations have demonstrated the successful application of chiral quark model to hadrons [35–41], hadron-hadron [42–46] and exotic multiquark [47–54] phenomenology.

On the other hand, recent years have seen remarkable progress of quantum simulation in quantum computers for a wide range of theoretical physics, such as lattice gauge theory & condensed-matter physics [55–57], Nuclear structure [58, 59], black holes [60–62], among others [63]. Quantum computers offer a unique opportunity to access real-time dynamics in quantum field theories, a regime that remains largely inaccessible to classical approaches. In particular, quantum simulation is expected to overcome the severe sign problem faced by lattice QCD, enabling studies of real-time phenomena [64–70] as well as the properties of dense quark matter [71–73].

* ayanendudutta@gmail.com

Despite this rapid progress, present-day quantum computers remain far from realizing full lattice QCD simulations. The large local Hilbert space associated with non-Abelian gauge fields, together with the intricate color dynamics and fermionic degrees of freedom, leads to qubit requirements and circuit depths that exceed the capabilities of current noisy intermediate-scale quantum (NISQ) devices. As a result, direct quantum simulations of exotic multiquark states, such as tetraquarks and pentaquarks, with fully dynamical gauge fields are presently out of reach. These limitations motivate the exploration of effective models and reduced descriptions that retain essential QCD features while remaining accessible to quantum simulation on near-term hardware. Here comes the chiral quark model as a promising alternative.

The chiral quark model provides a particularly suitable starting point for quantum simulation of tetraquark systems because it reduces the complexity of QCD to an explicit, few-body Hamiltonian while retaining the dominant low-energy quark–quark interactions relevant for multiquark binding. The model is formulated directly in terms of a nonrelativistic Hamiltonian with a small number of degrees of freedom: quark color, spin, flavor, and relative coordinates, leading to a drastically reduced Hilbert space compared to full lattice QCD with dynamical gauge fields. This compact structure enables an efficient mapping onto qubits and makes variational and real-time quantum algorithms feasible on near-term devices. Moreover, the Hamiltonian is explicitly known and parameterized, allowing direct construction of qubit operators without introducing auxiliary gauge constraints or large link-variable registers. Finally, the chiral quark model has direct contact with hadron phenomenology: it has been extensively benchmarked against meson, baryon, and multiquark spectra, so quantum simulations can be validated against established classical results. In this sense, the chiral quark model serves as an ideal intermediate platform, bridging phenomenologically relevant tetraquark physics and quantum-simulation techniques, while avoiding the prohibitive resource demands of full lattice QCD.

While classical chiral quark model analyses have provided valuable insights into the spectroscopy and internal structure of tetraquark systems [51–54], their extension to larger Hilbert spaces, fully coupled color configurations, and real-time multiquark dynamics is severely limited by computational complexity, thereby motivating quantum simulation as a natural and scalable framework to investigate the same tetraquark structures beyond the reach of classical methods.

In the present study, we investigate the double-bottom tetraquark bound and resonance states with quantum simulation in chiral quark model. The paper is arranged as follows: in Sec. II, we will summarize the chiral quark model and tetraquark wavefunctions, followed by the discussion on quantum simulation framework and quabit mapping in Sec. III. Sec. IV is devoted to results and discussions. Finally in Sec. (section ref.), we will briefly

present the concluding remarks.

II. THE CHIRAL QUARK MODEL

After several decades of development in high-energy physics, QCD-motivated quark models continue to play a central role in interpreting the multiquark candidates reported by experiments. In particular, the chiral quark model has demonstrated notable success in previous studies of hidden-charm pentaquark bound states with quantum numbers $IJ^P = \frac{1}{2}(\frac{1}{2})^\pm, \frac{1}{2}(\frac{3}{2})^\pm$, and $\frac{1}{2}(\frac{5}{2})^\pm$ [48], whose predicted properties were found to be compatible with the hidden-charm pentaquark structures observed by the LHCb Collaboration in 2015 [74]. This motivates the extension of the chiral quark model to the study of doubly-bottom tetraquark systems.

Within the complex scaling method, the four-body Hamiltonian is written as

$$H(\theta) = \sum_{i=1}^4 \left(m_i + \frac{\vec{p}_i^2}{2m_i} \right) - T_{\text{CM}} + \sum_{j>i=1}^4 V(\vec{r}_{ij} e^{i\theta}), \quad (1)$$

where the center-of-mass kinetic energy T_{CM} is subtracted to isolate the internal dynamics of the multiquark system. The interaction is modeled by a two-body potential,

$$V(\vec{r}_{ij} e^{i\theta}) = V_{\text{CON}}(\vec{r}_{ij} e^{i\theta}) + V_{\text{OGE}}(\vec{r}_{ij} e^{i\theta}) + V_\chi(\vec{r}_{ij} e^{i\theta}), \quad (2)$$

which includes the color-confining, one-gluon exchange, and Goldstone-boson exchange interactions. Since this work focuses on low-lying S -wave doubly-heavy tetraquark states, only the central and spin–spin components of the interaction are retained, while spin–orbit and tensor terms are neglected. The relative coordinates are complex rotated as $\vec{r} \rightarrow \vec{r} e^{i\theta}$, leading to the complex-scaled Schrödinger equation

$$[H(\theta) - E(\theta)] \Psi_{JM}(\theta) = 0. \quad (3)$$

According to the ABC theorem [75, 76], the complex-scaled Schrödinger equation in Eq. (3) admits three distinct types of eigenenergies: bound states, which appear on the negative real-energy axis below threshold; discretized continuum states, which are distributed along a branch cut rotated by an angle 2θ with respect to the real axis; and resonance states, which manifest as isolated poles above the continuum cut. The decay width of a resonance is given by $\Gamma = -2 \text{Im}(E)$.

We now briefly outline the interaction terms entering Eq. (2). Confinement, reflecting the non-Abelian nature of QCD, is known from lattice QCD studies to arise from multi-gluon exchanges, leading to a linearly rising potential between static color sources. At comparable distance scales, light-quark pair creation induces string breaking and flux-tube saturation [77]. These features are phenomenologically incorporated, for $\theta = 0^\circ$, through the

confinement potential

$$V_{\text{CON}}(\vec{r}_{ij}e^{i\theta}) = \left[-a_c(1 - e^{-\mu_c r_{ij}e^{i\theta}}) + \Delta \right] (\vec{\lambda}_i^c \cdot \vec{\lambda}_j^c), \quad (4)$$

where a_c , μ_c , and Δ are model parameters and $\vec{\lambda}^c$ denote the SU(3) Gell–Mann matrices. This interaction behaves linearly at short distances, with an effective string tension $\sigma = -a_c \mu_c (\vec{\lambda}_i^c \cdot \vec{\lambda}_j^c)$, and saturates to a constant value $(\Delta - a_c)(\vec{\lambda}_i^c \cdot \vec{\lambda}_j^c)$ at large separations.

The one-gluon-exchange (OGE) interaction, incorporating both Coulomb and color-magnetic contributions, is expressed as

$$V_{\text{OGE}}(\vec{r}_{ij}e^{i\theta}) = \frac{1}{4}\alpha_s(\vec{\lambda}_i^c \cdot \vec{\lambda}_j^c) \left[\frac{1}{r_{ij}e^{i\theta}} - \frac{1}{6m_i m_j} (\vec{\sigma}_i \cdot \vec{\sigma}_j) \frac{e^{-r_{ij}e^{i\theta}/r_0(\mu)}}{r_{ij}e^{i\theta} r_0^2(\mu)} \right], \quad (5)$$

where m_i and $\vec{\sigma}_i$ denote the quark mass and Pauli matrices, respectively. The contact term in the central potential is regularized in the complex-scaled coordinate as

$$\delta(\vec{r}_{ij}e^{i\theta}) \sim \frac{1}{4\pi r_0^2} \frac{e^{-r_{ij}e^{i\theta}/r_0}}{r_{ij}e^{i\theta}}, \quad (6)$$

with the regulator $r_0(\mu_{ij}) = \hat{r}_0/\mu_{ij}$ depending on the reduced mass μ_{ij} of the quark–(anti-)quark pair.

The effective strong coupling constant α_s is taken to be scale dependent and frozen at low energies, providing a unified description across light and heavy quark sectors. Following Ref. [78], it is parametrized as

$$\alpha_s(\mu_{ij}) = \frac{\alpha_0}{\ln\left(\frac{\mu_{ij}^2 + \mu_0^2}{\Lambda_0^2}\right)}, \quad (7)$$

where α_0 , μ_0 , and Λ_0 are model parameters.

The Goldstone-boson exchange terms can be written as:

$$V_\pi(\vec{r}_{ij}e^{i\theta}) = \frac{g_{ch}^2}{4\pi} \frac{m_\pi^2}{12m_i m_j} \frac{\Lambda_\pi^2}{\Lambda_\pi^2 - m_\pi^2} m_\pi \left[Y(m_\pi r_{ij}e^{i\theta}) - \frac{\Lambda_\pi^3}{m_\pi^3} Y(\Lambda_\pi r_{ij}e^{i\theta}) \right] (\vec{\sigma}_i \cdot \vec{\sigma}_j) \sum_{a=1}^3 (\lambda_i^a \cdot \lambda_j^a), \quad (8)$$

$$V_\sigma(\vec{r}_{ij}e^{i\theta}) = -\frac{g_{ch}^2}{4\pi} \frac{\Lambda_\sigma^2}{\Lambda_\sigma^2 - m_\sigma^2} m_\sigma \left[Y(m_\sigma r_{ij}e^{i\theta}) - \frac{\Lambda_\sigma}{m_\sigma} Y(\Lambda_\sigma r_{ij}e^{i\theta}) \right], \quad (9)$$

$$V_K(\vec{r}_{ij}e^{i\theta}) = \frac{g_{ch}^2}{4\pi} \frac{m_K^2}{12m_i m_j} \frac{\Lambda_K^2}{\Lambda_K^2 - m_K^2} m_K \left[Y(m_K r_{ij}e^{i\theta}) - \frac{\Lambda_K^3}{m_K^3} Y(\Lambda_K r_{ij}e^{i\theta}) \right] (\vec{\sigma}_i \cdot \vec{\sigma}_j) \sum_{a=4}^7 (\lambda_i^a \cdot \lambda_j^a), \quad (10)$$

| | | |
|------------------|--|--------|
| Quark masses | $m_u = m_d$ (MeV) | 313 |
| | m_b (MeV) | 5100 |
| Goldstone bosons | $\Lambda_\pi = \Lambda_\sigma$ (fm $^{-1}$) | 4.20 |
| | Λ_η (fm $^{-1}$) | 5.20 |
| | $g_{ch}^2/(4\pi)$ | 0.54 |
| | θ_P ($^\circ$) | -15 |
| Confinement | a_c (MeV) | 430 |
| | μ_c (fm $^{-1}$) | 0.70 |
| | Δ (MeV) | 181.10 |
| OGE | α_0 | 2.118 |
| | Λ_0 (fm $^{-1}$) | 0.113 |
| | μ_0 (MeV) | 36.976 |
| | \hat{r}_0 (MeV fm) | 28.170 |

TABLE I: Model parameters [51].

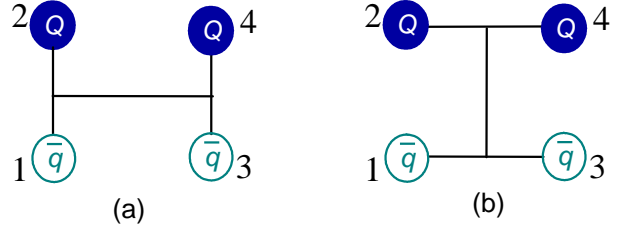


FIG. 1: Schematic for (a) meson-meson and (b) diquark-antidiquark configurations for double-bottom tetraquark ($Q = b$ and $q = u, d$).

$$V_\eta(\vec{r}_{ij}e^{i\theta}) = \frac{g_{ch}^2}{4\pi} \frac{m_\eta^2}{12m_i m_j} \frac{\Lambda_\eta^2}{\Lambda_\eta^2 - m_\eta^2} m_\eta \left[Y(m_\eta r_{ij}e^{i\theta}) - \frac{\Lambda_\eta^3}{m_\eta^3} Y(\Lambda_\eta r_{ij}e^{i\theta}) \right] (\vec{\sigma}_i \cdot \vec{\sigma}_j) \left[\cos \theta_p (\lambda_i^8 \cdot \lambda_j^8) - \sin \theta_p \right]. \quad (11)$$

Here, $Y(x) = e^{-x}/x$ is the standard Yukawa function. The physical η meson is incorporated by introducing the mixing angle θ_p rather than the pure octet state, with λ^a denoting the SU(3) flavor Gell–Mann matrices. The masses of the SU(3) Goldstone bosons, m_π , m_K , and m_η , are taken from their experimental values, while the σ -meson mass is fixed through the PCAC relation $m_\sigma^2 \simeq m_\pi^2 + 4m_{u,d}^2$ [79]. The chiral coupling constant g_{ch} is determined from the πNN coupling via $\frac{g_{ch}^2}{4\pi} = \frac{9}{25} \frac{g_{\pi NN}^2 m_{u,d}^2}{4\pi m_N^2}$, assuming exact SU(3) flavor symmetry, broken only by the strange-quark mass.

The chiral quark–(anti)quark interaction is active exclusively between light quark pairs and does not contribute to heavy–light or heavy–heavy sectors. All model parameters, summarized in Table I, are fixed a priori by reproducing established hadron [35–40], hadron–hadron [42–46], and multiquark [47–50] phenomenology.

At the quark level, QCD admits four fundamental degrees of freedom: color, flavor, spin, and spatial coordinates, so that the total wave function of a multi-quark system factorizes accordingly. For doubly-bottom tetraquarks of the form $QQ\bar{q}\bar{q}$ ($q = u, d$ and $Q = b$), two possible internal configurations are considered, as illustrated in Fig. 1: the meson–meson (MM) structure in Fig. 1(a) and the diquark–antidiquark (DA) structure in Fig. 1(b). Both configurations, as well as their mutual couplings, are included in the present analysis.

Compared to conventional hadrons, multi-quark systems allow a richer color structure. In the dimeson configuration, a colorless four-quark state may be constructed from either color-singlet or hidden-color channels, or from their coupling. Although it has been argued that the color-singlet channel alone can be sufficient when all excitations are included [80, 81], we adopt a more complete treatment by explicitly incorporating all relevant color structures and their couplings.

Within the color $SU(3)$ framework, the color wave functions of the color-singlet ($1 \otimes 1$) and hidden-color ($8 \otimes 8$) channels in the meson–meson configuration of Fig. 1(a) are denoted by χ_1^c and χ_2^c , respectively:

$$\chi_1^c = \frac{1}{3}(\bar{r}r + \bar{g}g + \bar{b}b) \otimes (\bar{r}r + \bar{g}g + \bar{b}b), \quad (12)$$

$$\begin{aligned} \chi_2^c = \frac{\sqrt{2}}{12} & (3\bar{b}r\bar{r}b + 3\bar{g}r\bar{r}g + 3\bar{b}g\bar{g}b + 3\bar{g}b\bar{b}g + 3\bar{r}g\bar{g}r \\ & + 3\bar{r}b\bar{b}r + 2\bar{r}r\bar{r}r + 2\bar{g}g\bar{g}g + 2\bar{b}b\bar{b}b - \bar{r}r\bar{g}g \\ & - \bar{g}g\bar{r}r - \bar{b}b\bar{g}g - \bar{b}b\bar{r}r - \bar{g}g\bar{b}b - \bar{r}r\bar{b}b). \end{aligned} \quad (13)$$

In addition, following the ordering indicated in Fig. 1, the color wave functions associated with the diquark–antidiquark configuration shown in Fig. 1(b) are denoted by χ_3^c and χ_4^c , corresponding to the color triplet–antitriplet ($3 \otimes \bar{3}$) and sextet–antisextet ($6 \otimes \bar{6}$) couplings, respectively:

$$\begin{aligned} \chi_3^c = \frac{\sqrt{3}}{6} & (\bar{r}r\bar{g}g - \bar{g}r\bar{r}g + \bar{g}g\bar{r}r - \bar{r}g\bar{g}r + \bar{r}r\bar{b}b \\ & - \bar{b}r\bar{r}b + \bar{b}b\bar{r}r - \bar{r}b\bar{b}r + \bar{g}g\bar{b}b - \bar{b}g\bar{g}b \\ & + \bar{b}b\bar{g}g - \bar{g}b\bar{b}g), \end{aligned} \quad (14)$$

$$\begin{aligned} \chi_4^c = \frac{\sqrt{6}}{12} & (2\bar{r}r\bar{r}r + 2\bar{g}g\bar{g}g + 2\bar{b}b\bar{b}b + \bar{r}r\bar{g}g + \bar{g}r\bar{r}g \\ & + \bar{g}g\bar{r}r + \bar{r}g\bar{g}r + \bar{r}r\bar{b}b + \bar{b}r\bar{r}b + \bar{b}b\bar{r}r \\ & + \bar{r}b\bar{b}r + \bar{g}g\bar{b}b + \bar{b}g\bar{g}b + \bar{b}b\bar{g}g + \bar{g}b\bar{b}g). \end{aligned} \quad (15)$$

For the flavor sector, the systems under consideration consist of two bottom quarks ($Q = b$) and two light antiquarks ($\bar{q} = \bar{u}, \bar{d}$), allowing only isospin $I = 0$ and 1 . The flavor wave functions are labeled as χ_{I,M_I}^f , and are given by

$$\chi_{0,0}^f = \sqrt{\frac{1}{2}}(\bar{u}b\bar{d}b - \bar{d}b\bar{u}b), \quad (16)$$

$$\chi_{1,-1}^f = \bar{u}b\bar{u}b, \quad (17)$$

where, without loss of generality, the third component of isospin M_I is chosen to be equal to the magnitude of the total isospin I , since the Hamiltonian does not distinguish between different M_I components.

We consider four-quark bound states with total spin $S = 0, 1$, and 2 . As the Hamiltonian does not contain spin–orbit interactions, the spin projection M_S can be taken equal to the total spin without loss of generality. The corresponding total spin wave functions χ_{S,M_S}^σ , constructed by coupling the spin wave functions of two sub-clusters using $SU(2)$ algebra, are given by

$$\chi_{0,0}^\sigma(4) = \chi_{00}^\sigma \chi_{00}^\sigma, \quad (18)$$

$$\chi_{0,0}^\sigma(4) = \frac{1}{\sqrt{3}}(\chi_{11}^\sigma \chi_{1,-1}^\sigma - \chi_{10}^\sigma \chi_{10}^\sigma + \chi_{1,-1}^\sigma \chi_{11}^\sigma), \quad (19)$$

$$\chi_{1,1}^\sigma(4) = \chi_{00}^\sigma \chi_{11}^\sigma, \quad (20)$$

$$\chi_{1,1}^\sigma(4) = \chi_{11}^\sigma \chi_{00}^\sigma, \quad (21)$$

$$\chi_{1,1}^\sigma(4) = \frac{1}{\sqrt{2}}(\chi_{11}^\sigma \chi_{10}^\sigma - \chi_{10}^\sigma \chi_{11}^\sigma), \quad (22)$$

$$\chi_{2,2}^\sigma(4) = \chi_{11}^\sigma \chi_{11}^\sigma, \quad (23)$$

where the two-body spin basis states are defined as

$$\chi_{11}^\sigma = \alpha\alpha, \chi_{1,-1}^\sigma = \beta\beta, \quad (24)$$

$$\chi_{10}^\sigma = \frac{1}{\sqrt{2}}(\alpha\beta + \beta\alpha), \quad (25)$$

$$\chi_{00}^\sigma = \frac{1}{\sqrt{2}}(\alpha\beta - \beta\alpha). \quad (26)$$

To solve the Schrödinger-like four-body bound-state problem, we employ the symmetry-preserving trial wavefunction. This wavefunction enforces the color singlet (or hidden-octet, triplet, sextet), spin singlet, and flavor symmetry sector through the quantum circuit ansatz. The spatial interactions of the four-quark state is incorporated with spatial transition characterized by the angle θ .

The identification of bound and resonance states of the double-bottom tetraquark will be produced by Variational Quantum Eigensolver (VQE) on the quantum circuit ansatz. The VQE optimized eigenvalues will serve as the bound or resonance states depending on the real or complex nature.

III. ENCODING TO QUBITS

In this section, we present the qubit encoding strategy adopted to map the chiral quark model Hamiltonian, introduced in the previous section, onto a quantum computing framework suitable for near-term quantum simulation. The encoding follows and extends our earlier work on quantum simulations of QCD-inspired models, tailored here to the doubly-heavy tetraquark sector. Our emphasis is on a transparent and physically motivated encoding of color, spin, and spatial degrees of freedom,

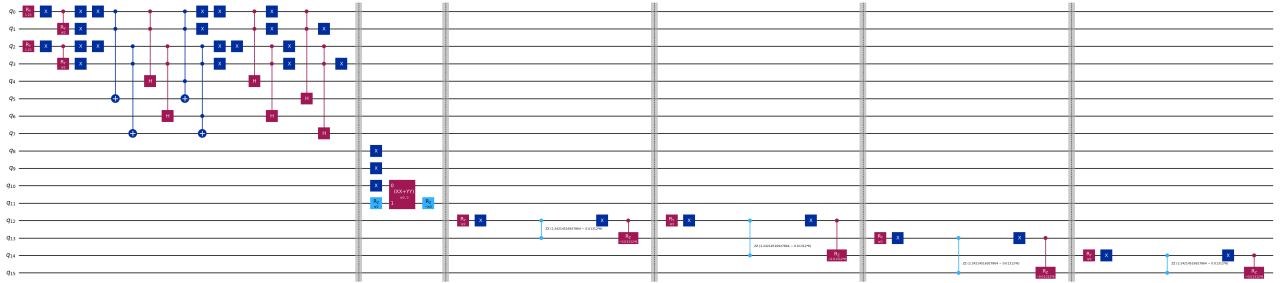


FIG. 2: The 16 qubit quantum circuit for MM configuration of double-bottom tetraquark. The first cell enforces color singlet-singlet projection, while the second cell projects spin $S = 0$. Last four cells assign spatial projection.

while deferring the explicit Pauli-string decomposition of the Hamiltonian to later stages of the simulation workflow.

- **Overview of the Qubit Register:**

The full tetraquark system is encoded using a total of 16 qubits. Each physical degree of freedom is mapped independently, allowing modular control over color, spin, and spatial structures:

- **Color sector:** 2 qubits are assigned to each quark to encode its color degree of freedom, resulting in 8 color qubits for the four-quark system.
- **Spin sector:** The spin of each quark is represented by a single qubit, contributing 4 qubits in total.
- **Spatial sector:** One qubit per quark is used to encode spatial information relevant for relative motion and potential terms, giving another 4 qubits.

This encoding yields a 16-qubit Hilbert space that captures the essential internal structure of the tetraquark system within an effective nonrelativistic framework.

- **Color Encoding and Multiquark Configurations:**

Color plays a central role in multiquark dynamics. For each quark, the color degree of freedom is encoded using two qubits according to

$$|00\rangle = |r\rangle, \quad |01\rangle = |g\rangle, \quad |10\rangle = |b\rangle, \quad |11\rangle = |\text{undefined}\rangle,$$

where the unphysical state $|11\rangle$ is excluded dynamically by the structure of the Hamiltonian and the quantum circuit constraints. This choice provides a minimal and hardware-efficient encoding of the SU(3) color space.

Within the 16-qubit register, the two distinct multiquark configurations: Meson–meson (MM) and Diquark–antidiquark (DA) are implemented. For the MM configuration, both color singlet–singlet and hidden-color octet–octet channels are incorporated in the quantum circuit. In the DA configuration, color triplet–antitriplet and sextet–antisextet channels are included. The coupling between these color sectors is realized through en-

tangling gates acting on the color qubits, enabling a fully coupled-channel description of the color dynamics.

An example quantum circuit enforcing the singlet–singlet color structure in the MM configuration is shown in Fig. 2. While the explicit gate sequence depends on the target hardware and compilation strategy, the circuit structure is designed to project the color wave function onto the desired irreducible representation of SU(3).

- **Spin Encoding and Total Spin Projection:**

The spin degree of freedom of each quark is encoded using a single qubit, with the computational basis representing spin-up and spin-down states. The total spin of the tetraquark system is enforced directly at the circuit level by preparing entangled spin states corresponding to definite total spin $S = 0, 1$, or 2 . In the example circuit shown in Fig. 2, the spin-singlet ($S = 0$) configuration is explicitly constructed.

This circuit-based enforcement of total spin avoids the need for post-selection and ensures that the variational quantum algorithms operate entirely within the physically relevant spin subspace. Spin-dependent interactions appearing in the chiral quark model Hamiltonian are then evaluated consistently within this restricted Hilbert space.

- **Spatial Encoding and Jacobi Coordinates:**

To encode spatial correlations and relative motion relevant for the potential terms, one qubit per quark is introduced to represent spatial degrees of freedom in an effective, discretized manner. Rather than encoding absolute particle positions, the spatial encoding is defined in terms of internal Jacobi coordinates, which naturally separate relative motion from center-of-mass dynamics.

For the encoding of spatial transition of quarks in the potential terms, the relative coordinate system denoted by the internal Jacobi coordinates are employed. For the meson–meson configuration shown in Fig. 1(a), they are

defined as

$$\vec{\rho} = \vec{x}_1 - \vec{x}_2, \quad (27)$$

$$\vec{\lambda} = \vec{x}_3 - \vec{x}_4, \quad (28)$$

$$\vec{R} = \frac{m_1 \vec{x}_1 + m_2 \vec{x}_2}{m_1 + m_2} - \frac{m_3 \vec{x}_3 + m_4 \vec{x}_4}{m_3 + m_4}, \quad (29)$$

while for the diquark–antidiquark configuration of Fig. 1(b), they read

$$\vec{\rho} = \vec{x}_1 - \vec{x}_3, \quad (30)$$

$$\vec{\lambda} = \vec{x}_2 - \vec{x}_4, \quad (31)$$

$$\vec{R} = \frac{m_1 \vec{x}_1 + m_3 \vec{x}_3}{m_1 + m_3} - \frac{m_2 \vec{x}_2 + m_4 \vec{x}_4}{m_2 + m_4}. \quad (32)$$

With these coordinate choices, the center-of-mass kinetic energy is exactly removed in the nonrelativistic framework.

In the quantum circuit, the Jacobi-coordinate dependence enters through controlled operations acting on the spatial qubits, ensuring that interquark potentials depend only on relative separations. This encoding is particularly advantageous for variational algorithms, as it minimizes redundant degrees of freedom and improves convergence toward physically meaningful states.

The flavor structure of the tetraquark enters only through fixed isospin assignments. Since no dynamical flavor-changing processes are considered, the flavor sector does not require additional qubits. Instead, isospin $I = 0$ or $I = 1$ contributes as a constant term in the Hamiltonian, determined by the chosen flavor configuration. This simplification significantly reduces qubit overhead while retaining the correct symmetry properties of the system.

The proposed 16-qubit encoding provides a balanced and physically grounded representation of the chiral quark model for doubly-heavy tetraquarks. By explicitly encoding color, spin, and spatial degrees of freedom and enforcing the MM and DA configurations at the circuit level, the approach captures essential nonperturbative QCD features while remaining compatible with current quantum hardware. This framework serves as a foundation for variational quantum simulations of multiquark bound and resonant states in effective QCD-inspired models.

IV. RESULTS AND DISCUSSIONS

In this work, we present a systematic study of the low-lying S -wave spectrum of doubly-heavy tetraquark systems of the form $QQ\bar{q}\bar{q}$, with $q = u, c$ and $Q = b$. Both meson–meson and diquark–antidiquark configurations are explicitly incorporated in the analysis, allowing for a fully coupled-channel description of the tetraquark

dynamics. Under the assumption that all relative orbital angular momenta l_1 , l_2 , and l_3 vanish, the resulting tetraquark states possess positive parity. Consequently, the total angular momentum J is entirely determined by the total spin S of the system and can take the values $J = S = 0, 1$, or 2 .

The numerical results of our calculations are summarized in Table II, where we present the masses and dominant components of the lowest-lying doubly-heavy tetraquark candidates in the S -wave channels with $J^P = 0^+$ and 1^+ . For each state, the table reports the complex scaling angle θ used in the calculation, the corresponding lowest eigenenergy, the binding energy measured relative to the relevant two-hadron threshold, and, where applicable, the decay width extracted from the imaginary part of the complex eigenvalue.

In particular, Table II provides a detailed decomposition of the wave-function components for possible bound states in the doubly-bottom sector, obtained within a complete coupled-channel framework in which all accessible color, spin, and spatial channels consistent with a given set of quantum numbers IJ^P are taken into account. In the present exploratory study, we focus on two representative quantum-number assignments, namely $I(J^P) = 0(0^+)$ and $0(1^+)$, which are expected to host the most deeply bound configurations. A more comprehensive investigation of additional spin and isospin channels is currently in progress and will be reported elsewhere.

The first column of the Table II lists the identification of possible bound or resonance states; the following two columns present the complex scale angle and theoretical mass (M) of the tetraquark state. The last two columns show the binding energy (E_B) or decay width for the bound or resonance states respectively.

In the present analysis, we focus on the $B^{(*)}-\bar{B}^{*0}$ meson–meson channels as well as the $(bb)^{(*)}(\bar{u}\bar{d})^{(*)}$ diquark–antidiquark configurations, which constitute natural analogues of other doubly-heavy tetraquark systems. Our coupled-channel calculations indicate that possible bound and resonant structures emerge exclusively in the isoscalar channel with quantum numbers $I(J^P) = 0(1^+)$. The inclusion of heavier bottom quarks significantly enhances the attraction in the system, leading to the formation of deeply bound states in the color-singlet components of the $B-\bar{B}^{*0}$ and $B^{*}-\bar{B}^{*0}$ channels. The corresponding binding energies are found to be -59.185 MeV and -40.449 MeV, respectively.

These sizable binding energies point to a strong interaction mechanism dominated by the color-singlet meson–meson configuration in the $B^{(*)}-\bar{B}^{*0}$ system. After incorporating the appropriate mass shifts associated with the constituent hadron thresholds, the resulting masses of the doubly-bottom tetraquark bound states are estimated to be 10545 MeV and 10563 MeV, respectively. These values place the states well below the corresponding open-bottom thresholds, reinforcing their interpretation as genuine bound states.

| States | θ | Mass M (MeV) | Binding energy E_B (MeV) | Decay width $-\Gamma/2$ (MeV) |
|-----------|----------|----------------|----------------------------|-------------------------------|
| Resonance | 39.311 | 10813.5 | - | -15.3 |
| Bound | 0 | 10563.851 | -40.449 | 0 |
| Resonance | 22.70 | 10818.3 | - | -5.26 |
| Resonance | 172.306 | 10699.64 | - | -28.5 |
| Bound | 0 | 10545.115 | -59.185 | 0 |
| Resonance | 140.13 | 10827.03 | - | 0.193 |
| Resonance | 0 | 10716.41 | - | 1.43 |
| Resonance | 0 | 10587.86 | - | 1.116 |

TABLE II: Lowest lying states of double-bottom tetraquarks $bb\bar{q}\bar{q}$ with quantum numbers $I(J^P) = 0(0^+)$ and $0(1^+)$. The two bound states $B^{*-}\bar{B}^{*0}$ and $B^-\bar{B}^{*0}$ are identified with binding energy ~ -40 and ~ -59 MeV.

Following the analysis strategy of Ref. [51], we verify that the bound-state energies remain stable under variations of the complex scaling angle θ , which provides a nontrivial consistency check of their physical nature within the complex scaling framework. For resonant states, the decay widths are extracted from the imaginary parts of the complex eigenvalues and encode the coupling strength to open scattering channels.

Although the meson–meson color-singlet channel provides the dominant contribution to the bound-state wave functions, hidden-color components play a non-negligible role. Their inclusion leads to modest energy shifts and induces quantitative changes in the resonance widths, highlighting the importance of employing a complete color basis in coupled-channel calculations. This interplay between color-singlet and hidden-color configurations is essential for a reliable description of both bound and resonant doubly-bottom tetraquark states.

V. CONCLUSION

In summary, this work constitutes the first explicit realization of tetraquark bound and resonant states within

a quantum simulation framework, demonstrating the feasibility of encoding and probing multiquark dynamics on quantum hardware. Beyond reproducing static spectral properties, the present approach opens a new avenue for systematically improving quantitative predictions and for investigating the interplay of different color configurations in a genuinely quantum setting. In particular, the framework developed here lays the groundwork for accessing real-time color dynamics, which remains inaccessible in conventional classical treatments.

Future work will focus on implementing the color-dynamical Hamiltonian on quantum simulators and exploring time-dependent phenomena, as well as extending the present study to other doubly heavy systems.

[1] B. Aubert *et al.* (BABAR Collaboration), Phys. Rev. Lett. **95**, 142001 (2005).
[2] S. -K. Choi *et al.* (Belle Collaboration), Phys. Rev. Lett. **100**, 142001 (2008).
[3] T. Aaltonen *et al.* (CDF Collaboration), Phys. Rev. Lett. **102**, 242002 (2009).
[4] M. Ablikim *et al.* (BESIII Collaboration), Phys. Rev. Lett. **110**, 252001 (2013).
[5] V. Khachatryan *et al.* (CMS Collaboration), J. High Energ. Phys. **05**, 013 (2017).
[6] L. C. Bland *et al.* (ANDY Collaboration), arXiv: 1909.03124 [nucl-ex].
[7] R. Aaij *et al.* (LHCb Collaboration), J. High Energ. Phys. **10**, 086 (2018).
[8] A. V. Berezhnay, A. V. Luchinsky and A. A. Novoselov, Phys. Rev. D **86**, 034004 (2012).
[9] A. Esposito and A. D. Polosa, Eur. Phys. J. C **78**, 782 (2018).
[10] M. N. Anwar, J. Ferretti, F. -K. Guo, E. Santopinto and B. -S. Zou, Eur. Phys. J. C **78**, 647 (2018).
[11] M. A. Bedolla, J. Ferretti, C. D. Roberts and E. Santopinto, arXiv: 1911.00960 [hep-ph].
[12] Z. -G. Wang, Eur. Phys. J. C **77**, 432 (2017).
[13] W. Chen, H. -X. Chen, X. Liu, T. G. Steele and S. -L. Zhu, Phys. Lett. B **773**, 247 (2017).
[14] Y. Bai, S. Lu and J. Osborne, Phys. Rev. B **798**, 134930 (2019).
[15] W. Heupel, G. Eichmann and C. S. Fischer, Phys. Lett. B **718**, 545 (2012).
[16] V. R. Debastiani and F. S. Navarra, Chin. Phys. C **43**, 013105 (2019).
[17] A. V. Berezhnay, A. K. Likhoded, A. V. Luchinsky and

A. A. Novoselov, Phys. Rev. D **84**, 094023 (2011).

[18] M. Karliner, S. Nussinov and J. L. Rosner, Phys. Rev. D **95**, 034011 (2017).

[19] J. -M. Richard, A. Valcarce and J. Vijande, Phys. Rev. D **95**, 054019 (2017).

[20] J. Wu, Y. -R. Liu, K. Chen, X. Liu and S. -L. Zhu, Phys. Rev. D **97**, 094015 (2018).

[21] X. Chen, Eur. Phys. J. A **55**, 106 (2019).

[22] M. -S. Liu, Qi -F. Lü and X. -H. Zhong and Q. Zhao, Phys. Rev. D **100**, 016006 (2019).

[23] G. -J. Wang, L. Meng and S. -L. Zhu, arXiv: 1907.05177 [hep-ph].

[24] J. -M. Richard, A. Valcarce and J. Vijande, Phys. Rev. C **97**, 035211 (2018).

[25] C. Hughes, E. Eichten and C. T. H. Davies, Phys. Rev. D **97**, 054505 (2018).

[26] E. J. Eichten and C. Quigg, Phys. Rev. Lett. **119**, 202002 (2017).

[27] M. Karliner and J. L. Rosner, Phys. Rev. Lett. **119**, 202001 (2017).

[28] E. Hernández, J. Vijande, A. Valcarce and Jean-Marc Richard, arXiv: 1910.13394 [hep-ph].

[29] C. E. Fontoura, G. Krein, A. Valcarce and J. Vijande, Phys. Rev. D **99**, 094037 (2019).

[30] J. Carlson, L. Heller and J. A. Tjon, Phys. Rev. D **37**, 744 (1988).

[31] D. Ebert, R. N. Faustov, V. O. Galkin and W. Lucha, Phys. Rev. D **76**, 114015 (2007).

[32] L. Leskovec, S. Meinel, M. Pflaumer and M. Wagner, Phys. Rev. D **100**, 014503 (2019).

[33] A. Francis, R. J. Hudspith, R. Lewis and K. Maltman, Phys. Rev. Lett. **118**, 142001 (2017).

[34] P. Junnarkar, N. Mathur and M. Padmanath, Phys. Rev. D **99**, 034507 (2019).

[35] J. Vijande, F. Fernandez and A. Valcarce, J. Phys. **G31**, 481 (2005).

[36] A. Valcarce, F. Fernández, P. Gonzalez and V. Vento, Phys. Lett. B **367**, 35 (1996).

[37] J. Segovia, D. R. Entem and F. Fernandez, Phys. Lett. B **662**, 33 (2008).

[38] J. Segovia, A. M. Yasser, D. R. Entem and F. Fernández, Phys. Rev. D **78**, 114033 (2008).

[39] P. G. Ortega, J. Segovia, D. R. Entem and F. Fernández, Phys. Rev. D **94**, 114018 (2016).

[40] G. Yang, J. Ping and J. Segovia, Few-Body Syst. **59**, 113 (2018).

[41] G. Yang, J. Ping, P. G. Ortega and J. Segovia, arXiv: 1904.10166 [hep-ph].

[42] F. Fernandez, A. Valcarce, U. Straub and A. Faessler, J. Phys. G **19**, 2013 (1993).

[43] A. Valcarce, F. Fernández, A. Buchmann and A. Faessler, Phys. Rev. C **50**, 2246 (1994).

[44] P. G. Ortega, J. Segovia, D. R. Entem and F. Fernández, Phys. Rev. D **81**, 054023 (2010).

[45] P. G. Ortega, J. Segovia, D. R. Entem and F. Fernández, Phys. Rev. D **94**, 074037 (2016).

[46] P. G. Ortega, J. Segovia, D. R. Entem and F. Fernández, Phys. Rev. D **95**, 034010 (2017).

[47] J. Vijande, A. Valcarce and K. Tsushima, Phys. Rev. D **74**, 054018 (2006).

[48] G. Yang and J. Ping, Phys. Rev. D **95**, 014010 (2017).

[49] G. Yang and J. Ping, Phys. Rev. D **97**, 034023 (2018).

[50] G. Yang, J. Ping and J. Segovia, Phys. Rev. D **99**, 014035 (2019).

[51] G. Yang, J. Ping and J. Segovia, Phys. Rev. D **101** (2020) no.1, 014001 [arXiv:1911.00215 [hep-ph]].

[52] G. Yang, J. Ping and J. Segovia, Phys. Rev. D **103** (2021) no.7, 074011 [arXiv:2101.04933 [hep-ph]].

[53] Y. K. Chen, W. L. Wu, L. Meng and S. L. Zhu, Phys. Rev. D **109** (2024) no.1, 014010 [arXiv:2310.14597 [hep-ph]].

[54] X. H. Zheng, Y. Ma and S. L. Zhu, [arXiv:2510.01505 [hep-ph]].

[55] E. Zohar, challenges and methods,” Phil. Trans. A. Math. Phys. Eng. Sci. **380** (2021) no.2216, 20210069 [arXiv:2106.04609 [quant-ph]].

[56] D. Gonzalez-Cuadra, M. Hamdan, T. V. Zache, B. Braverman, M. Kornjaca, A. Lukin, S. H. Cantu, F. Liu, S. T. Wang and A. Keesling, *et al.* Nature **642** (2025) no.8067, 321-326 [arXiv:2410.16558 [quant-ph]].

[57] J. C. Halimeh, N. Mueller, J. Knolle, Z. Papić and Z. Davoudi, [arXiv:2509.03586 [quant-ph]].

[58] A. Pérez-Obiol, A. M. Romero, J. Menéndez, A. Rios, A. García-Sáez and B. Juliá-Díaz, Sci. Rep. **13**, 12291 (2023)

[59] M. J. Savage, EPJ Web Conf. **296** (2024), 01025 [arXiv:2312.07617 [nucl-th]].

[60] E. Rinaldi, X. Han, M. Hassan, Y. Feng, F. Nori, M. McGuigan and M. Hanada, PRX Quantum **3** (2022) no.1, 010324 [arXiv:2108.02942 [quant-ph]].

[61] Y. H. Shi, R. Q. Yang, Z. Xiang, Z. Y. Ge, H. Li, Y. Y. Wang, K. Huang, Y. Tian, X. Song and D. Zheng, *et al.* Nature Commun. **14** (2023) no.1, 3263 [arXiv:2111.11092 [quant-ph]].

[62] V. I. Kolobov, K. Golubkov, J. R. Muñoz de Nova and J. Steinhauer, Nature Phys. **17** (2021) no.3, 362-367 [arXiv:1910.09363 [gr-qc]].

[63] I. M. Georgescu, S. Ashhab and F. Nori, Rev. Mod. Phys. **86** (2014), 153 [arXiv:1308.6253 [quant-ph]].

[64] E. A. Martinez, C. A. Muschik, P. Schindler, D. Nigg, A. Erhard, M. Heyl, P. Hauke, M. Dalmonte, T. Monz and P. Zoller, *et al.* Nature **534** (2016), 516-519 [arXiv:1605.04570 [quant-ph]].

[65] N. Klco, J. R. Stryker and M. J. Savage, Phys. Rev. D **101** (2020) no.7, 074512 [arXiv:1908.06935 [quant-ph]].

[66] D. E. Kharzeev and Y. Kikuchi, Phys. Rev. Res. **2** (2020) no.2, 023342 [arXiv:2001.00698 [hep-ph]].

[67] S. V. Mathis, G. Mazzola and I. Tavernelli, Phys. Rev. D **102** (2020) no.9, 094501 [arXiv:2005.10271 [quant-ph]].

[68] Z. Y. Zhou, G. X. Su, J. C. Halimeh, R. Ott, H. Sun, P. Hauke, B. Yang, Z. S. Yuan, J. Berges and J. W. Pan, Science **377** (2022) no.6603, abl6277 [arXiv:2107.13563 [cond-mat.quant-gas]].

[69] J. Mildenberger, W. Mruczkiewicz, J. C. Halimeh, Z. Jiang and P. Hauke, Nature Phys. **21** (2025) no.2, 312-317 [arXiv:2203.08905 [quant-ph]].

[70] Y. Y. Atas, J. F. Haase, J. Zhang, V. Wei, S. M. L. Pfaendler, R. Lewis and C. A. Muschik, Phys. Rev. Res. **5** (2023) no.3, 033184 [arXiv:2207.03473 [quant-ph]].

[71] A. Yamamoto, Phys. Rev. D **104** (2021) no.1, 014506 [arXiv:2104.10669 [hep-lat]].

[72] A. Tomiya, [arXiv:2205.08860 [hep-lat]].

[73] A. M. Czajka, Z. B. Kang, Y. Tee and F. Zhao, [arXiv:2210.03062 [hep-ph]].

[74] R. Aaij *et al.* [LHCb], Phys. Rev. Lett. **115** (2015), 072001 [arXiv:1507.03414 [hep-ex]].

[75] J. Aguilar and J. M. Combes, Commun. Math. Phys. **22**

(1971), 269-279

[76] E. Balslev and J. M. Combes, Commun. Math. Phys. **22** (1971), 280-294

[77] G. S. Bali *et al.* [SESAM], Phys. Rev. D **71** (2005), 114513 [arXiv:hep-lat/0505012 [hep-lat]].

[78] J. Segovia, D. R. Entem, F. Fernandez and E. Hernandez, Int. J. Mod. Phys. E **22** (2013), 1330026 [arXiv:1309.6926 [hep-ph]].

[79] M. D. Scadron, Phys. Rev. D **26** (1982), 239-247

[80] M. Harvey, Nucl. Phys. A **352** (1981), 326-342

[81] J. Vijande, A. Valcarce and N. Barnea, Phys. Rev. D **79** (2009), 074010 [arXiv:0903.2949 [hep-ph]].